

Vanadium dioxide : A Peierls-Mott insulator stable against disorder

Cédric Weber*,¹ David D. O'Regan,^{1,2} Nicholas D. M. Hine,^{1,3}
Mike C. Payne,¹ Gabriel Kotliar,⁴ and Peter B. Littlewood^{1,5}

¹*Cavendish Laboratory, University of Cambridge,
J. J. Thomson Avenue, Cambridge CB3 0HE, United Kingdom*

²*Theory and Simulation of Materials, École Polytechnique Fédérale de Lausanne,
Station 12, 1015 Lausanne, Switzerland*

³*The Thomas Young Centre and the Departments of Materials and Physics,
Imperial College London, London SW7 2AZ, United Kingdom*

⁴*Rutgers University, 136 Frelinghuysen Road, Piscataway, NJ, U.S.A.*

⁵*Physical Sciences and Engineering, Argonne National Laboratory, Argonne, Illinois 60439, U.S.A.*

Vanadium dioxide (VO_2) undergoes a first order metal-insulator transition (MIT) at 340 K [1]. At high temperature, the crystal structure is metallic with the rutile structure (R), while it transforms to the monoclinic (M_1) phase and becomes insulating below the transition temperature. Experimental evidence [2] suggests that the insulator is obtained due to strong correlations in this material, however density functional theory (DFT) predicts the M_1 phase to be metallic [3, 4]. In this work, we develop and carry out state of the art linear scaling DFT calculations refined with non-local dynamical mean-field theory (DMFT). We validate our approach by applying this cutting edge methodology to the M_1 phase of VO_2 . We find that a Peierls-Mott instability is responsible for the insulating M_1 phase, which furthermore survives a large degree of disorder accounting for the MIT observed [5] when no long-range crystallographic order is present. The Peierls-Mott instability involves two electrons per vanadium atom in t_{2g} orbitals and reconciles the Peierls picture with recent soft x-ray absorption spectroscopy (XAS) [6], which points towards a breaking of the one electron per 3d orbital picture suggested early by Goodenough [7]. Finally, since fluctuations in VO_2 thin film deposition may cause departure from the ideal stoichiometry [8], we discuss how the MIT is affected by oxygen vacancies.

The nature of the metal-insulator (MIT) transition in VO_2 has been long discussed, with particular emphasis placed on the role of electron correlations in forming the charge gap. Photoemission experiments give strong evidence for strong electron-electron and electron-phonon coupling in VO_2 [2], suggesting that this compound is an archetypal Mott insulator. An alternative point of view is that the low-temperature phase of VO_2 may constitute a band (Peierls) insulator, where the crystal distortion with the V-V dimerization splits the a_{1g} bonding band. Lastly one should consider a charge transfer insulator exhibiting a strong mass renormalisation. The purpose of

this paper is to disentangle these competing pictures.

The Peierls picture was supported from a first-principles perspective using LDA+GW calculations, where the authors found that dynamical effects combined with off-diagonal matrix elements in the self-energy opened a gap [4], although the value of the fundamental gap was there predicted to be almost zero and thus well below the experimental value of 0.6 eV [9]. Very recently, a model Hamiltonian approach using cluster DMFT applied to a three band Hamiltonian for the t_{2g} orbitals has been shown to successfully capture the insulating nature of the M_1 phase [10, 11], and the authors found a charge gap of 0.6 eV, in very good agreement with experiment [9]. Hence, VO_2 is, in the latter view, not a conventional Mott insulator. Instead, the formation of dynamical V-V singlet pairs due to strong Coulomb correlations is necessary to trigger the opening of a Peierls gap. We note, however, that in Ref. [10] the vanadium 3d subshell is occupied by a single electron (0.8 electrons for the a_{1g} with only 0.1 electrons remaining in each of the $e_{\pi g}$ orbitals). A general problem with model Hamiltonian approaches, recently pointed out in Ref. [12], is that the 3d orbital density is very much affected by the orbital subset projection used in the calculations. In particular, it has been shown recently using XAS measurements [6] that the states of VO_2 are not well characterized by a single dominant ionic configuration, rather exhibiting a distributed orbital character, suggesting room for correction of Goodenough's ionic picture of VO_2 .

The key issues that we address in this work are: (1) Is the $3d^1$ ionic picture of Goodenough valid and how many electrons are involved in the orbital selection process; (2) Can Mott correlations alone drive VO_2 to an insulator, and what is the minimal local repulsion U_d necessary to localize the charge, i.e., the Zaanen-Sawatzky-Allen (ZSA) boundary [13, 14]; (3) How is the ZSA boundary affected by other localization processes, such as the Anderson charge localization induced by disorder, and can we find an insulator for a combination of realistic disorder and Coulomb repulsion; (4) Are non-local corrections to the self energy (the Peierls mechanism) an essential ingredient to trigger the gap opening for reasonable local

repulsion U_d , and is the latter insulating phase stable against external perturbations such as disorder.

To address these points, we move beyond the model Hamiltonian approach and investigate the effect of correlations in a disordered prototype for the metal-insulator transition (MIT) in VO_2 from the ab-initio perspective. We study the M_1 phase of VO_2 using first-principles calculations as a function of static disorder with a state of the art linear scaling DFT method [15]. The capability of linear scaling DFT to describe large super-cells, containing several hundreds of atoms, is necessary to comprehensively tackle the issue of disorder. We extend our DFT calculations with the dynamical mean-field theory (DMFT) approximation [16, 17] in order to refine the description of the strong correlations induced by the 3d subshell of the vanadium sites (for more details see the supplementary material). Throughout this work we used typical values for the screened Coulomb interaction ($U = 4$ eV) and Hund's coupling ($J = 0.68$ eV) [18, 19], and our calculations were carried out for 324 atom super-cells (108 V atoms) and 768 atom super-cells (256 V atoms) at fixed temperature $T = 189$ K. All orbitals are defined in the local coordinate system [20] associated with the vanadium atoms.

We first discuss single-site DMFT calculations for paramagnetic VO_2 . The dependence of the spectral function on the on-site repulsion U_d is shown in Fig. 1. We find that the M_1 phase of VO_2 is metallic for $U_d = 4$ eV and that there is a large spectral weight present at the Fermi level. Hence, VO_2 is described by DFT+DMFT as a charge transfer correlated paramagnetic metal, with a moderate mass renormalization $m^*/m = 1.35$, of the same order as the mass renormalization in the rutile phase obtained by other groups ($m^*/m = 1.8$ from Ref. [3] and $m^*/m = 1.51$ from Ref. [10]). The large spectral weight at the Fermi level in Fig. 1 is of predominantly d_{xy} character, the contribution from the e_g orbitals being negligible: the spin-independent orbital densities at the Fermi level $\rho_\sigma(\epsilon_F)$ are 0.02, 0.02, 0.19, 0.25, 0.28 for, respectively, $d_{x^2-y^2}, d_{3z^2-r^2}, d_{yz}, d_{xz}, d_{xy}$ symmetry, which indicates a strong selection of the t_{2g} orbitals at the Fermi level in agreement with the orbital selection scenario argued long ago by Goodenough [7]. Notably, we find that the dynamical correlations, described by the imaginary part of the self-energy, also suggest that the d_{xy} orbital is the most correlated orbital, whereas the e_g states are weakly correlated (for more details see Fig. 2 and Fig. 3 of the supplementary material).

However, our results deviate from the description of Goodenough. In particular, we obtain a vanadium 3d sub-shell filling of $n = 3.15$ electrons from DFT, much larger than the $3d^1$ configuration of the ionic picture. We emphasize that we used a set of local Wannier orbitals, variationally optimized during the energy minimization carried out in the DFT calculations [21], which renders the calculation of the electronic density very re-

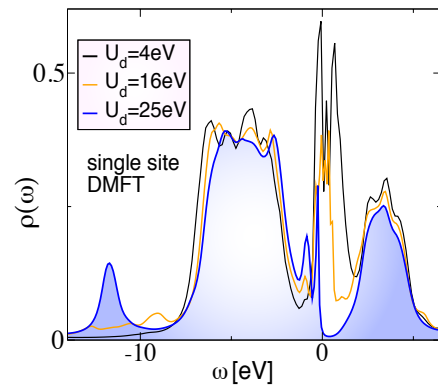


FIG. 1: **ZSA boundary:** (Color online) Dependence of the spectral function $\rho(\omega)$ with respect to the Coulomb repulsion U_d .

liable. Larger 3d orbital occupations in VO_2 than the single electron have been reported in earlier DFT calculations (LSDA+ U finds $n = 2.48$ e [6]). We note, furthermore, that similar occupancies are obtained for the R phase, both by experimental measurement ($n = 1.78$ e from XAS [6]) and DFT calculations (LSDA+ U finds $n = 2.31$ e [6] and LMTO-ASA gives $n = 3.35$ e [22]).

For larger U_d , we find that the spectral weight at the Fermi level shrinks, and we obtain an insulator for $U_d = 25$ eV, placing VO_2 well below the ZSA boundary U_d^c , estimated between 21 eV and 25 eV. Since we obtain a paramagnetic insulator only for Coulomb repulsions of the order of the atomic limit, this strongly suggests that Mott correlations alone are not responsible for the insulating state of the M_1 phase, as also suggested by early LDA calculations [20, 23] which failed to reproduce the insulating state. We conclude that a large 3d-3d Coulomb interaction alone is not sufficient to generate a large band gap for VO_2 . Finally, we also explored the dependence on the Hund's coupling J and found no significant change in the mass renormalization by varying J between 0.3 eV and 1.2 eV, for fixed $U_d = 4$ eV, although increasing J enhances the mass renormalization for $U_d = 8$ eV and $U_d = 16$ eV.

If Coulomb correlations alone cannot lead to insulating behavior, perhaps the inevitable disorder due to imperfections of the crystal, or self-trapping due to strong electron-phonon coupling could be relevant. Hence we applied a random three-dimensional Gaussian displacement to both the V and O atomic sites. The Gaussian width δ characterizes the amplitude of the disorder. We also note that a large number of uncontrolled and uncorrelated experimental parameters, such as the variation of the atomic positions due to the shear induced by dislocations, are described at the theoretical level by a Gaussian distribution (central limit theorem). Notwithstanding, we use a single representation of disorder for each

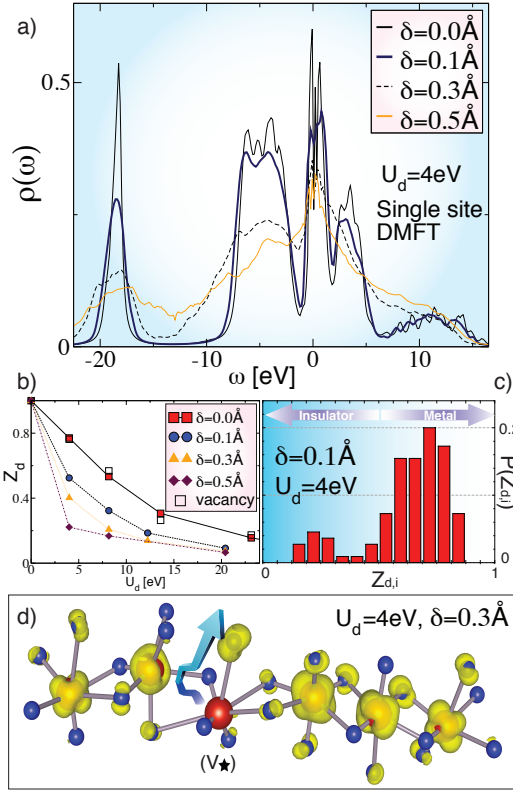


FIG. 2: **Anderson and Mott localization:** (Color online) a) Spectral function ρ of paramagnetic VO_2 in the presence of Gaussian disorder δ . b) Averaged quasi-particle weight Z_d with respect to the repulsion U_d for zero ($\delta = 0 \text{ \AA}$) to large disorder ($\delta = 0.5 \text{ \AA}$). Calculations including a single O vacancy in the $\delta = 0 \text{ \AA}$ case are also shown for comparison (open squares). c) Distribution of the local quasi-particle weight $Z_{d,i}$ for $\delta = 0.1 \text{ \AA}$. d) Isosurface of the real space representation of the Fermi density for disorder $\delta = 0.3 \text{ \AA}$. The large (small) sphere denotes V (O) atoms along the rutile axis.

amplitude δ , Gaussian disorder satisfying the ergodicity theorem such that the local average over different configurations is equivalent to the average over space for large enough super-cells.

The spectral function for disordered VO_2 is shown in Fig. 2.a. Although the spectral weight at the Fermi level is suppressed with increasing disorder (reflecting charge localisation) the system remains metallic up to the largest physical amplitudes of disorder. The effect of the localization induced by disorder is also observed in the averaged quasi-particle weight Z_d (Fig. 2.b) and in the spatial distribution of the local quasi-particle weight $Z_{d,i}$ (Fig. 2.c), which clearly shows that the disorder generates regions in the crystal with strong localization, which coexist with metallic parts of the crystal where the localization has only a weak effect. These droplets of strongly correlated Fermi liquid generate a larger mass renormalization m^*/m on average, as observed in the decrease of

the averaged quasi-particle weight ($Z_d = m/m^*$) as the disorder increases (Fig. 2.b).

The localization effect can be understood in a simple picture: when the O atoms move closer to the V atomic site, the static charge repulsion induces a larger charge transfer energy $\Delta = \epsilon_d - \epsilon_p$, which enhances the strength of the correlation locally (the repulsion U of the one band Hubbard model translates into the charge transfer energy in d-p theories [13]). This effect is illustrated in Fig. 2.d, where we show an isosurface of the real-space representation of the Fermi density $\rho(\epsilon_F, r)$ for one of the V chains along the rutile axis for $\delta = 0.3 \text{ \AA}$, where large (small) spheres denote V (O) atomic sites. The V atom highlighted by a star has two very near oxygen neighbors, which is expected to induce a larger charge transfer energy. The latter results in a transfer of charge from the vanadium site to one of its oxygen neighbors (indicated by an arrow). The subtle interplay between the localization induced by the disorder (Anderson-like) and the localization induced by strong correlations (Mott-like) is captured by the DFT+DMFT methodology.

We now move to the non-local cluster cellular DMFT calculations (c-DMFT). The non-local correlation present in cluster DMFT drives VO_2 to an insulator (Fig. 3.a), in agreement with earlier DMFT calculations using model Hamiltonians [10] and we obtain a gap of $\sim 0.6 \text{ eV}$ in agreement with both the latter and the experimental value [9]. We did not observe any finite size effect, and the Peierls gaps obtained extracted from the 324 and 768 atom super-cells are identical. We find that large disorder quenches the Peierls state for $\delta > 0.1 \text{ \AA}$. Very interestingly, the insulating Peierls state survives for moderate disorder $\delta = 0.1 \text{ \AA}$, although the gap is reduced down to $\sim 0.3 \text{ eV}$. We also carried out cluster DMFT calculations for the case of a single O vacancy: the O vacancy creates a mid-gap state (inset of Fig. 3.a), spatially localized in the center of the three V atoms surrounding the vacancy, as illustrated by the real space representation of the Fermi level density (Fig. 3.b) but does not strongly affect the band edges. In conclusion, our results suggest that the Peierls instability in VO_2 is very robust, surviving external perturbations such as reduction of the long-range crystallographic order or local impurities.

The imaginary part of the self-energy of the dynamical Peierls singlet is shown in Fig. 3.c. We observe that the gap is mainly induced by dynamical correlations in the d_{xy} orbital, which exhibit a pole at the Fermi level. In our view, the dynamical V-V dimers generate a Mott instability (the mechanism may be thus termed Peierls-Mott). In particular, the spectral weight (inset) shows that the cluster DMFT almost entirely depletes the d_{yz} orbital, leaving two electrons equally shared between the d_{xz} and d_{xy} orbitals. The lobe of the latter orbitals point towards the rutile axis, whereas the d_{yz} orbital is oriented perpendicular to this direction and thus the latter does

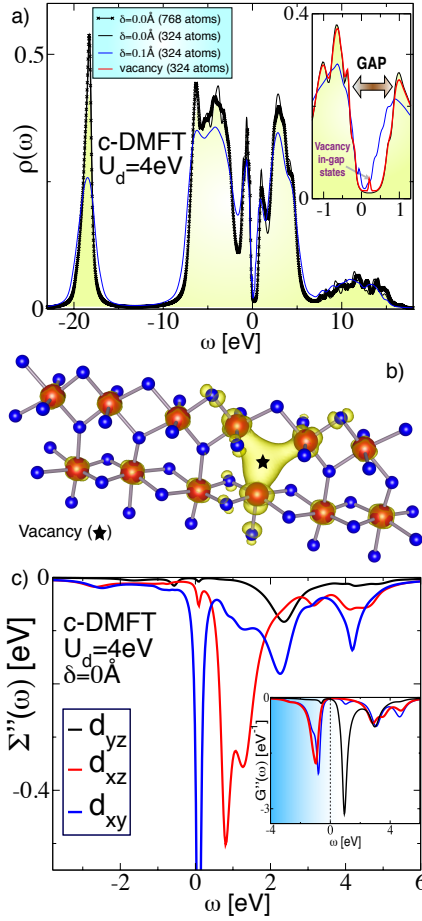


FIG. 3: **Mott-Peierls instability:** (Color online) a) Spectral function ρ obtained using cellular cluster DMFT (c-DMFT) calculations without ($\delta = 0$ Å) disorder for moderate (324 atom) and large (768 atom) super-cells. Calculations for disordered VO_2 ($\delta = 0.1$ Å) and for a single O vacancy are also shown for comparison. Inset: Enlargement of the low energy scale, the gap of ~ 0.6 eV is shown. The vacancy introduces a mid-gap state, highlighted by the arrow. b) Isosurface of the real space representation of the charge density at the Fermi level for calculations for an O vacancy (star). The large (small) sphere denotes V (O) atoms along the rutile axis (horizontal direction). c) Imaginary part of the self-energy and (inset) imaginary part of the Green's function for $\delta = 0$ Å.

not contribute strongly to the orbital bonding within a V-V dimer.

Interestingly, therefore in our picture we find that two electrons per V atom lie in bonding orbitals, leading to a strong Mott dynamical divergence in the self-energy (Peierls-Mott). This contrasts with the picture of Ref. [10], where a single electron on each V is of bonding character and the repulsion U_d drives the bonding orbitals to a singlet configuration, following the early proposal of Sommers and Doniach [24]. In the latter picture, the repulsion energy may be dramatically reduced by the

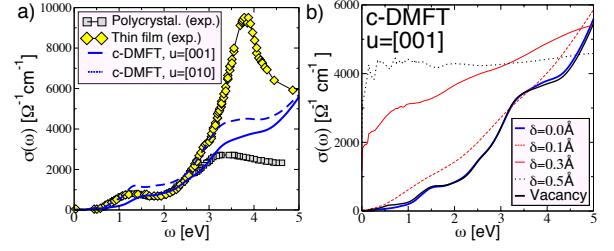


FIG. 4: **Optical spectra:** (Color online) a) Theoretical optical conductivity along the rutile axis (solid lines) and along the perpendicular direction (dashed lines) calculated with cellular DMFT. Experimental data for polycrystalline films [26] (squares) and thin films (diamonds) [27] are shown for comparison. b) Optical conductivity along the rutile axis obtained by cellular DMFT for disordered VO_2 for various disorder amplitudes δ .

formation of the singlet state, manifested in the fact that the low-frequency behavior of the on-site component of the self-energy, that associated with the a_{1g} orbital, is linear in frequency, as opposed to a Mott insulator in which Σ'' diverges. In our picture, orbital rehybridization acts to deplete the d_{yz} orbital, leaving 2 e in two orbitals per V site, in turn generating a Mott instability which creates a pole in the local self-energy (Peierls-Mott). We note that this result reconciles the Peierls scenario with recent XAS [6] and photoemission spectroscopy measurements [25], which hint at an occupation of $n \approx 2$ for the 3d sub-shell in the M_1 phase.

Finally, the optical conductivity calculated using cluster DMFT (Fig. 4.a) is in qualitative agreement with experimental data obtained for polycrystalline films [26] and thin films [27]. We note that the optical gap is not dramatically affected by a moderate degree of disorder $\delta = 0.1$ Å (Fig. 4.b). For large disorder, however, VO_2 is a bad metal and we note, in particular, that no Drude peak is obtained in the optical conductivity, and that the disorder induces strong oscillations in the optical response for the infrared frequency range $\omega < 1$ eV.

In conclusion, we have carried out linear scaling first principle calculations, in combination with cluster DMFT, on VO_2 , both with and without disorder. We find that VO_2 is a Peierls-Mott insulator, and that the ZSA boundary of the paramagnetic insulator is obtained only for unrealistic values of the Coulomb repulsion ($U_d \approx 25$ eV). We propose a new mechanism for the insulating M_1 phase of VO_2 based on an orbital selective Mott transition, assisted by the Peierls distortion: the Peierls instability involves an orbital selection, and bonds the d_{xy} and d_{xz} orbitals along the rutile axis, filling each orbital with one electron, and in turn generates a Mott instability. This scenario may be described as *Peierls assisted orbital selective Mott transition*. Finally, we demonstrated that the Peierls phase survives

moderate Gaussian disorder ($\delta = 0.1 \text{ \AA}$), and hence our picture accounts for the observation of the MIT in the experimentally realistic, disordered system [5]. Whether the critical temperature associated to the Mott instability is lower than the structural phase transition temperature (SPT), and whether this picture accounts for the recent observation of metallic responses in VO_2 in the M_1 phase near the SPT [28] remains to be seen. Finally, we found that oxygen vacancies induce a localized mid-gap state, leaving the band edges unaffected, shedding some light on thin-film measurements where substrate strain can induce stoichiometric modification [8]. Our results, combining lattice disorder and a powerful method for describing non-local, dynamical correlation, open up new frontiers for first principles materials design under realistic experimental conditions.

C.W. and D.D.O'R and N.D.M.H contributed codes; C.W. and D.D.O'R carried out the calculations; C.W. and D.D.O'R proposed the project; all authors contributed to the writing of the paper.

The authors declare no competing financial interests. We are grateful to Kristjan Haule for sharing his CTQMC code. C.W. was supported by the Swiss National Foundation for Science (SNFS). D.D.O'R. was supported by EPSRC and the National University of Ireland. N.D.M.H was supported by EPSRC grant number EP/G055882/1. P.B.L is supported by the US Department of Energy under FWP 70069. Correspondence and requests for materials should be addressed to C.W.

-
- [1] F. J. Morin, Phys. Rev. Lett. **3**, 34 (1959).
 - [2] K. Okazaki, H. Wadati, A. Fujimori, M. Onoda, Y. Muraoka, and Z. Hiroi, Phys. Rev. B **69**, 165104 (2004).
 - [3] A. Belozarov, A. Poteryaev, and V. Anisimov, JETP Letters **93**, 70 (2011).
 - [4] R. Sakuma, T. Miyake, and F. Aryasetiawan, Journal of Physics: Condensed Matter **21**, 064226 (2009).
 - [5] F. Chudnovskii and G. Stefanovich, Journal of Solid State Chemistry **98**, 137 (1992).
 - [6] M. W. Haverkort, Z. Hu, A. Tanaka, W. Reichelt, S. V. Streltsov, M. A. Korotin, V. I. Anisimov, H. H. Hsieh, H.-J. Lin, C. T. Chen, D. I. Khomskii, and L. H. Tjeng, Phys. Rev. Lett. **95**, 196404 (2005).
 - [7] J. B. Goodenough, J. Solid State Chem. **3**, 490 (1971).
 - [8] C. Chen, Y. Zhao, X. Pan, V. Kuryatkov, A. Bernussi, M. Holtz, and Z. Fan, Journal of Applied Physics **110**, 023707 (2011).
 - [9] T. C. Koethe, Z. Hu, M. W. Haverkort, C. Schüßler-Langeheine, F. Venturini, N. B. Brookes, O. Tjernberg, W. Reichelt, H. H. Hsieh, H.-J. Lin, C. T. Chen, and L. H. Tjeng, Phys. Rev. Lett. **97**, 116402 (2006).
 - [10] S. Biermann, A. Poteryaev, A. I. Lichtenstein, and A. Georges, Phys. Rev. Lett. **94**, 026404 (2005).
 - [11] B. Lazarovits, K. Kim, K. Haule, and G. Kotliar, Phys. Rev. B **81**, 115117 (2010).
 - [12] X. Wang, M. J. Han, L. de Medici, C. A. Marianetti, and A. J. Millis, arXiv/1110.2782.
 - [13] J. Zaanen, G. A. Sawatzky, and J. W. Allen, Phys. Rev. Lett. **55**, 418 (1985).
 - [14] W. F. Brinkman and T. M. Rice, Phys. Rev. B **2**, 4302 (1970).
 - [15] C.-K. Skylaris, P. D. Haynes, A. A. Mostofi, and M. C. Payne, Journal of Physics: Condensed Matter **17**, 5757 (2005).
 - [16] A. Georges, G. Kotliar, W. Krauth, and M. J. Rozenberg, Rev. Mod. Phys. **68**, 13 (1996).
 - [17] T. A. Maier, T. Pruschke, and M. Jarrell, Phys. Rev. B **66**, 075102 (2002).
 - [18] M. Korotin, N. Skorikov, and V. Anisimov, The Physics of Metals and Metallography **94**, 17 (2002).
 - [19] W. E. Pickett, S. C. Erwin, and E. C. Ethridge, Phys. Rev. B **58**, 1201 (1998).
 - [20] V. Eyert, Ann. Phys. (Leipzig) **11**, 650 (2002).
 - [21] C.-K. Skylaris, A. A. Mostofi, P. D. Haynes, O. Diéguez, and M. C. Payne, Phys. Rev. B **66**, 035119 (2002).
 - [22] M. Guelfucci, Journal of Physics and Chemistry of Solids **62**, 1961 (2001).
 - [23] R. M. Wentzcovitch, W. W. Schulz, and P. B. Allen, Phys. Rev. Lett. **72**, 3389 (1994).
 - [24] C. Sommers and S. Doniach, Solid State Comm. **28**, 133 (1978).
 - [25] R. Zimmermann, P. Steiner, R. Claessen, F. Reinert, S. Hüfner, P. Blaha, and P. Dufek, Journal of Physics: Condensed Matter **11**, 1657 (1999).
 - [26] M. M. Qazilbash, K. S. Burch, D. Whisler, D. Shrekenhamer, B. G. Chae, H. T. Kim, and D. N. Basov, Phys. Rev. B **74**, 205118 (2006).
 - [27] K. Okazaki, S. Sugai, Y. Muraoka, and Z. Hiroi, Phys. Rev. B **73**, 165116 (2006).
 - [28] M. M. Qazilbash, A. Tripathi, A. A. Schafgans, B.-J. Kim, H.-T. Kim, Z. Cai, M. V. Holt, J. M. Maser, F. Keilmann, O. G. Shpyrko, and D. N. Basov, Phys. Rev. B **83**, 165108 (2011).

Vanadium dioxide : A Peierls-Mott insulator stable against disorder. Supplementary material

Cédric Weber*,¹ David D. O'Regan,^{1,2} Nicholas D. M. Hine,^{1,3}
Mike C. Payne,¹ Gabriel Kotliar,⁴ and Peter B. Littlewood^{1,5}

¹*Cavendish Laboratory, University of Cambridge,
J. J. Thomson Avenue, Cambridge CB3 0HE, United Kingdom*

²*Theory and Simulation of Materials, École Polytechnique Fédérale de Lausanne,
Station 12, 1015 Lausanne, Switzerland*

³*The Thomas Young Centre and the Departments of Materials and Physics,
Imperial College London, London SW7 2AZ, United Kingdom*

⁴*Rutgers University, 136 Frelinghuysen Road, Piscataway, NJ, U.S.A.*

⁵*Physical Sciences and Engineering, Argonne National Laboratory, Argonne, Illinois 60439, U.S.A.*

METHODOLOGY

Kohn-Sham density-functional theory (DFT) [1, 2] has been shown to be capable of making accurate predictions for many materials. DFT combines high accuracy and moderate computational cost, yet the computational effort required to perform calculations with conventional DFT approaches is still non negligible: it increases with the cube of the number of atoms, rendering them unable to routinely tackle problems comprising more than a few hundred atoms, even on modern large supercomputers. Since the pioneering work of the Nobel laureate Walter Kohn [3], it has been known that it is possible to reformulate DFT to exploit the short-ranged nature of quantum mechanics, so that the computational cost scales linearly which would, in principle, allow calculations with many thousands of atoms. The ONETEP approach [4–6], used in this work, is an example of the practical realization of linear-scaling DFT and DFT+ U , and is particularly notable for its accuracy equivalent to a plane-wave method, by means of its *in situ* optimization of a set of local Wannier orbitals with a respect to a systematically improvable basis.

The linear scaling performance of ONETEP allowed us to study large atomic super-cells. Specifically, we investigated both a moderate supercell of 324 atoms for VO₂ (108 V atoms) and a large supercell of 768 atoms (256 V atoms). We used, for the crystallographic structure of the M₁ phase of VO₂, the lattice constants and atomic positions obtained for powder VO₂ ($a = 5.743$ Å, $b = 4.517$ Å, $c = 5.375$ Å, and $\beta = 122.6^\circ$) since the lattice parameters of thin films vary with charge localization and substrate-induced built-in strain [7]. The electronic core states were represented by GGA scalar-relativistic pseudo-potentials generated with the OPIUM package [8]. The (3s,3p,3d,4s) and (2s,2p) atomic shells were respectively treated as valence states for the V and O atoms. Hence, we used 10 orbitals to describe each V atom and 4 to describe each O atom, giving a total of 1944 orbitals for the 324 atom super-cell and 4608 for the 768 atom super-cell.

ONETEP [4] is at the cutting edge of developments in first principles calculations. However, while the fundamental difficulties of performing accurate first-principles calculations with linear-scaling cost have been solved, one remaining problem of DFT approaches in general is that conventional approximations to the exchange-correlation (XC) functions fail in describing many compounds where strong correlations are present. In such cases, DFT often predicts moments and energetics that are qualitatively inconsistent with experiment, or fails to describe the insulating state and converges to a metallic state instead. DFT+DMFT is a computationally moderately expensive method for refining the description of on-site Coulomb interactions provided by such XC functionals and, hence, for extending the range of applicability of DFT to strongly-correlated materials.

The principle of DFT+DMFT is to separate the dominant subspace of the system, which is well-described by conventional XC functionals due to its delocalized and free-electron character, from a subset of localized subspaces, so-called *correlated sites*, which are strongly correlated and not adequately described by the XC functionals. The XC correlated sites are then explicitly augmented with screened Coulomb and Hund's coupling interactions within these sites, together with a double-counting term to correct for the component already included within the DFT XC functional.

The correlated sites are typically spanned by a set of 3d and/or 4f atomic-like orbitals, which define a set of localized Hubbard projectors [9]. Solutions of appropriate orbital symmetry of the hydrogenic Schrödinger equation, such as atomic-like or linear muffin-tin orbitals, are the most common choice [10–12] for Hubbard projectors. The vanadium-centered correlated sites were delineated in our calculations using hydrogenic 3d orbitals as Hubbard projectors, characterized by the canonical Clementi-Raimondi [13] effective charge of $Z = 8.9829$ for this atomic sub-shell and species, determining their spatial diffuseness.

In the implementation of the linear-scaling DFT method used in this work, we work with the single-

particle density-matrix, which is expressed in a separable form [14, 15] [45]:

$$\rho(\mathbf{r}, \mathbf{r}') = \sum_{\alpha\beta} \phi_{\alpha}(\mathbf{r}) K^{\alpha\beta} \phi_{\beta}(\mathbf{r}'), \quad (1)$$

where $\{\phi_{\alpha}\}$ is a set of localized nonorthogonal generalized Wannier functions (NGWFs) variationally optimized during the energy minimization carried out as part of the DFT calculations [16]. The density kernel $K^{\alpha\beta} = \langle \phi^{\alpha} | \hat{\rho} | \phi^{\beta} \rangle$ is the representation of the single-particle density operator $\hat{\rho}$ in terms of the contravariant NGWF duals $\{\phi^{\alpha}\}$, defined as those which satisfy the relationship $\langle \phi^{\alpha} | \phi_{\beta} \rangle = \delta_{\alpha\beta}$. The NGWFs are, in turn, expanded in terms of a systematic basis of Fourier-Lagrange, or psinc functions [17]. The size of this basis is determined by a plane-wave kinetic energy cutoff (a minimum of 822 eV for all reciprocal lattice vectors in our calculations). The DFT energy functional is iteratively minimized with respect to both the density kernel and the NGWF expansion coefficients using a minimization scheme which is detailed in Ref. [18]. Therefore, the NGWFs are a readily accessible set of localized orbitals (spatially truncated to atom-centered spheres of radius 6.6 Å) which are calculated with linear-scaling computational cost. No additional approximation such as the density kernel truncation was used in this work, and the energy convergence was tested against the plane-wave kinetic energy cutoff and the spatial truncation of the NGWFs.

Once the fully converged energy minimization of VO₂ was carried out, the full Green's function was computed in the finite temperature Matsubara representation [46] from the readily available DFT Hamiltonian \mathbf{H} :

$$G^{\alpha\beta}(i\omega_n) = ((i\omega_n + \mu)S_{\alpha\beta} - H_{\alpha\beta} - \Sigma_{\alpha\beta})^{-1}, \quad (2)$$

where μ is the chemical potential (fixed at the mid-energy between the last occupied state of the ONETEP calculation and the first empty state), \mathbf{S} is the full overlap matrix between the NGWFs so that $\phi_{\alpha} = S_{\alpha\beta}\phi_{\beta}$ and Σ is the self-energy matrix computed by the DMFT algorithm. We note that the computation of the Green's function requires large matrix inversion (in particular, for VO₂, the matrix to invert is of size 1944×1944 for the 324 atom super-cell and 4608×4608 for the 768 atom super-cell. These super-cells allowed us to describe spatially dependent perturbations, such as static disorder (see Fig. 1), and also to consider oxygen vacancies [47]. Matrix inversion was carried out for 100 Matsubara frequencies to provide converged sampling of the Green's function. To achieve reasonable computational time, we performed the matrix inversion on recently-developed graphical computational units (GPUs) using a home-made parallel implementation of the Cholesky LU decomposition with the CUDA programming language. The calculations were carried out using 8 GPUs in parallel,

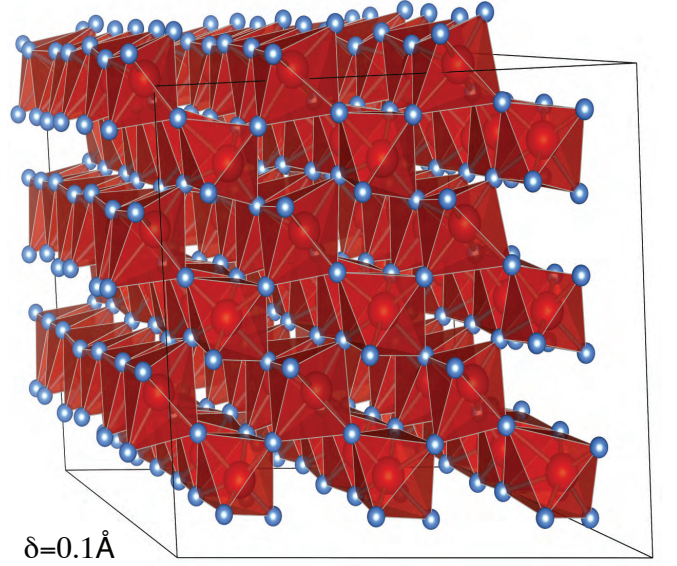


FIG. 1: **Super-cell for DFT+DMFT calculations:** (Color online) Super-cell used for the 324 atom DFT+DMFT calculations for disordered VO₂ with $\delta = 0.1$ Å.

achieving a total of 4000 GFLOPS (giga floating-point operations per second), allowing a tremendous speed-up of Green's function calculation (the computational time needed to carry out the matrix products and matrix inversions involved in the calculation for a 100 Matsubara frequencies was of the order of a few minutes for the largest super-cell). The matrix multiplications involved throughout the DMFT calculations were also performed using the CUDA architecture.

The projected Green's function $\tilde{\mathbf{G}}$ of the vanadium 3d correlated sites is obtained as

$$\tilde{G}_{mm'}^{(I)}(i\omega_n) = W_{m\alpha}^{(I)} G^{\alpha\beta}(i\omega_n) V_{\beta m'}^{(I)}, \quad (3)$$

where I runs over the Vanadium atoms, m and m' over the five atomic 3d orbitals used as orthonormal Hubbard projectors (in real cubic-harmonic notation: $d_{x^2-y^2}$, $d_{3z^2-r^2}$, d_{yz} , d_{xz} , d_{xy}), α and β are the indices for the NGWFs, and the matrices $V_{\alpha m}^{(I)} = \langle \phi_{\alpha} | \varphi_m^{(I)} \rangle$ and $W_{m\alpha}^{(I)} = \langle \varphi_m^{(I)} | \phi_{\alpha} \rangle$ are the overlap between the NGWFs $\{\phi_{\alpha}\}$ and the hydrogenic orbital $\{\varphi_m^{(I)}\}$ at the Vanadium site I and with orbital index m . Note that the orthonormality of the Hubbard projectors implies that we do not need to distinguish them from their duals (the generalization to nonorthogonal projectors is discussed in Ref [19]).

The strong correlation acting within each Vanadium site is described by the conventional Slater-Kanamori

form of the interaction term [20, 21], namely

$$\mathcal{H}_{int} = U_d \sum_m n_{m\uparrow} n_{m\downarrow} + (U'_d - \frac{J}{2}) \sum_{m>m'} n_m n_{m'} \quad (4)$$

$$- J \sum_{m>m'} \left(2S_m S_{m'} + \left(d_{m\uparrow}^\dagger d_{m\downarrow}^\dagger d_{m'\uparrow} d_{m'\downarrow} \right) \right),$$

for each correlated site and with no inter-site interactions, where the first term describes the effect of intra-orbital Coulomb repulsion U_d and the second term describes the inter-orbital repulsion U'_d . The latter is renormalized by J in order to ensure rotational invariance of the interaction (for a review see Ref. [22]). The third term is the Hund's rule coupling, described by a spin exchange of amplitude J . \mathbf{S}_m denotes the spin of orbital m , $S_m = \frac{1}{2} d_{ms}^\dagger \boldsymbol{\sigma}_{ss'} d_{ms'}$, where $\boldsymbol{\sigma}$ is the vector of Pauli matrices indexed by s and s' . Generally, the hierarchy of interactions is $U_d > U'_d > J$. U_d and J were set to typical values for the screened interactions for VO_2 , namely $U_d = 4\text{eV}$ and $J = 0.68\text{eV}$ [23, 24].

The interaction term (4), combined with (2) and (3), defines a local problem at each Vanadium site I of the lattice, which we solve with the DMFT algorithm [25]. In the single site DMFT approach, the projected self-energy matrix $\tilde{\Sigma}^{(I)(J)}$ is assumed to be local, i.e.,

$$\tilde{\Sigma}^{(I)(J)} = 0 \quad (5)$$

for non-local Vanadium site indices ($I \neq J$), unlike the cluster cellular DMFT [26] (c-DMFT) approach where spatial non-local contributions from vanadium sites belonging to the same dimer are included.

The self-energy is obtained by solving an auxiliary Anderson impurity problem (AIM) for each V atom (V-V dimer) in the single DMFT (cluster DMFT). The hybridization matrix Δ in the orbital subspace ($d_{x^2-y^2}$, $d_{3z^2-r^2}$, d_{yz} , d_{xz} , d_{xy}) of the AIM problem is defined, for each site, as:

$$\Delta(i\omega_n) = (i\omega_n + \mu) \tilde{\mathbf{O}} - \tilde{\Sigma} - \mathbf{E}^{\text{imp}} - \tilde{\mathbf{G}}^{-1}, \quad (6)$$

$\tilde{\mathbf{O}}$ is the local projected overlap matrix, which is related to the non-orthogonality of the DFT basis set (NGWFs) [27–29] and $\tilde{\mathbf{O}} = \mathbf{1}$ in the particular case of orthonormal Hubbard projectors in the form of Kohn-Sham Wannier functions. In particular, we find that $\tilde{\mathbf{O}}$ is related to the NGWF's overlap matrix by

$$\tilde{\mathbf{O}}_{mm'}^{(I)} = \left(W_{m\alpha}^{(I)} (S^{-1})^{\alpha\beta} V_{\beta m'}^{(I)} \right)^{-1}. \quad (7)$$

The static part of the hybridisation function $\mathbf{E}^{\text{imp}} = \Delta(i\omega_n \rightarrow \infty)$ defines the energy levels of the impurity in the absence of hybridisation (atomic limit). Both $\tilde{\mathbf{O}}$ and \mathbf{E}^{imp} define the impurity problem and they are constructed such that the hybridization matrix $\Delta(i\omega_n)$ exhibits the correct physical decay \propto

$1/i\omega_n$ at large frequency (we ensured that $\tilde{\mathbf{O}}_{mm'}^{(I)} = \lim_{\omega \rightarrow \infty} \left[\tilde{\mathbf{G}}^{-1}(i\omega)'' / \omega \right]$ to a high precision, as required by this condition). The self-energy $\tilde{\Sigma}$ is obtained by solving the Anderson impurity problem defined by the hybridization (6) and the interaction Hamiltonian (4).

The AIM is solved using two different solvers: (1) a finite temperature Lanczos algorithm [30–32], and some of the results were cross-checked and benchmarked with (2) a continuous-time Monte Carlo solver (CTQMC) [33, 34]. The two solvers both suffer from approximations but complement each other: the Lanczos solver uses a finite discretization of the hybridization (6) and suffers from finite size effects. The CTQMC solver suffers from the so-called *fermionic quantum sign problem* when the off-diagonal elements are considered, hence in this work we neglect within the CTQMC implementation the off-diagonal elements of the hybridization matrix (6). We note, however, that the amplitude of the off-diagonal elements depends strongly on the choice of the localized Hubbard projectors, and, in particular, they depend on the choice for the local orientation of the local ($\mathbf{e}_x, \mathbf{e}_y, \mathbf{e}_z$) axis. The off-diagonal elements of the hybridization and Green's function prove to be small for the vanadium 3d set employed in this work when the local coordinates defined for VO_2 are used (see discussion hereafter).

Once the local self-energy $\tilde{\Sigma}$ is obtained, it is up-folded to the space spanned by the Kohn-Sham orbitals (equivalently the space spanned by NGWFs), in the separable form

$$\Sigma_{\alpha\beta} = \sum_{I,J} V_{\alpha m}^{(I)} \tilde{\Sigma}_{mm'}^{(I)(J)} W_{m'\beta}^{(J)}. \quad (8)$$

As pointed out recently in [35], the separable form of the projectors of the self-energy enforces the causality of the up-folded self-energy (the local self-energy in the Hubbard projector basis is causal by construction, so that $\tilde{\Sigma}_{mm}^{(I)(I)}(i\omega_n)'' \leq 0$, $\forall (i\omega_n, m, I)$, since it is obtained by solving the AIM in the local orthogonal hydrogenic basis). We note that the causality is a necessary requirement to obtain physical observables. We carefully checked that all of the obtained self-energies were causal, since numerical error might still induce some unexpected fluctuation in the imaginary part of the self-energy).

One particular difficulty arises when one wants to construct a non-interacting Hamiltonian H from the DFT-LDA ground-state density. Since the LDA already contains the influence of the Coulomb interaction to a certain degree, the problem of double counting of these contributions by the interaction Hamiltonian (4) arises. In order to avoid this double counting, one has to subtract off the interaction contributions from the LDA. Unfortunately, the precise form for a particular set of orbitals is not known and the best one can do is to account for these contributions in an averaged way. In this work, we used

the canonical form of the correction E_{dc} , given by

$$E_{\text{dc}} = U_d^{av} (n_d - 0.5) - \frac{J}{2} (n_d - 1), \quad (9)$$

where n_d is the total occupancy of the vanadium 3d subspace, as defined by the Hubbard projectors, and U_d^{av} is the averaged repulsion related to the intra-orbital and inter-orbital repulsion, computed as follows [36]:

$$U_d^{av} = \frac{U_d + 2(N_{\text{deg}} - 1)U'_d}{2N_{\text{deg}} - 1} \quad (10)$$

and N_{deg} is given by the number of orbitals.

The unfolded self-energy, in the covariant NGWFs representation, is hence corrected by E_{dc} , giving

$$\Sigma_{\alpha\beta} = \sum_{IJ} V_{\alpha m}^{(I)} \left(\tilde{\Sigma}_{mm'}^{(I)(J)} - E_{\text{dc}} \delta_{mm'}^{(I)(J)} \right) W_{m'\beta}^{(J)}. \quad (11)$$

The double-counting correction avoids spurious artifacts, such as a shift of the subspace occupancies when the Coulomb interaction U_d is increased from zero. In this work, we did not find any significant deviation from the DFT density in the DFT+DMFT scheme, providing a strong indication that the double-counting term (9) correctly accounts for interactions already included in the DFT-LDA Hamiltonian \mathbf{H} .

For the particular case of VO_2 in the M_1 phase, due to the buckling of the V atoms, it is convenient to carry out the DMFT in a rotated basis, making use of a local coordinate system associated with the vanadium sites. In particular, the rotation used in this work is such that the local e_x axis is directed towards the rutile axis and the local e_y axis points towards the in-plane oxygen. The vanadium-apical oxygen vector forms a 90° angle with the rutile axis [37]. This allows us to obtain an hybridization matrix (6), which is as diagonal as possible. This is crucial for the CTQMC algorithm, since it neglects the off-diagonal terms. The rotation is carried out in orbital space [38] and translates for the projected Green's function as follows:

$$\tilde{\mathbf{G}}^{\text{rot}} = \tilde{\mathbf{U}}^\dagger \tilde{\mathbf{G}} \tilde{\mathbf{U}}, \quad (12)$$

where $\tilde{\mathbf{U}}$ is the 5×5 rotation matrix in cubic harmonic space, corresponding to a real space rotation $R^{(3)}$, and $\tilde{\mathbf{G}}^{\text{rot}}$ is the rotated Green's function. The same holds for the projected self-energy obtained by solving the AIM model $\tilde{\Sigma}^{\text{rot}}$, which is rotated back to the original system of coordinates:

$$\tilde{\Sigma} = \tilde{\mathbf{U}} \tilde{\Sigma}^{\text{rot}} \tilde{\mathbf{U}}^\dagger. \quad (13)$$

Equations (2), (3), (6) and (11) are iterated until DMFT convergence is obtained. Real frequency quantities are readily available from the Lanczos solver and provides us

access to the physical observables of the system. In particular, the density of states is available from the retarded full Green's function:

$$\rho(\omega) = \rho^{\alpha\beta}(\omega) S_{\beta\alpha}, \quad (14)$$

where the NGWF-resolved spectral density $\rho_{\alpha\beta}(\omega)$ is defined by the retarded Green's function obtained at the DMFT self-consistency $\mathbf{G}_{\mathbf{R}}$ as:

$$\rho^{\alpha\beta}(\omega) = \frac{G_R^{\alpha\beta}(\omega) - G_R^{\dagger\alpha\beta}(\omega)}{2i\pi}. \quad (15)$$

A very common experimental probe is optical spectroscopy, which is accessed in this work through the optical conductivity. The optical conductivity in DFT+DMFT is computed by using the Kubo formula of linear response theory in the *no-vertex-corrections* [48] approximation [39], via the expression

$$\sigma(\omega) = \frac{2\pi e^2 \hbar}{\Omega} \int d\omega' \frac{f(\omega' - \omega) - f(\omega')}{\omega} \times (\rho^{\alpha\beta}(\omega' - \omega) \mathbf{v}_{\beta\gamma} \rho^{\gamma\delta}(\omega') \mathbf{v}_{\delta\alpha}), \quad (16)$$

where the factor two accounts for the spin degeneracy, Ω is the simulation-cell volume, e the electron charge, \hbar the reduced Planck constant, $f(\omega)$ is the Fermi-Dirac distribution, and the optical conductivity is obtained by the convolution of charge density matrix operator $\rho^{\alpha\beta}$, defined in equation (15), and the bare vertex $\mathbf{v}_{\alpha\beta}$ is given for a non-orthogonal basis by [40]

$$\mathbf{v}_{\alpha\beta} = \mathbf{p}/m_e = -i\hbar/m_e \langle \phi_\alpha | \nabla | \phi_\beta \rangle. \quad (17)$$

We emphasize that the so-called *Peierls substitution* [39] approximation was not used here.

Another interesting physical quantity probed in this work is the quasi-particle weight of a local vanadium 3d subspace $Z_{d,i}^m$, where the index i runs over the Vanadium site and m over the d orbitals. We used the discrete Eliashberg estimate to obtain the quasi-particle weight:

$$Z_{d,i}^m = \left(1 - \frac{\tilde{\Sigma}_{mm}^{\prime(i)(i)}(i\omega_1)}{\omega_1} \right)^{-1}, \quad (18)$$

where ω_1 is the first Matsubara frequency. The quasi-particle weight $Z_{d,i}$ of the Vanadium site i is estimated by the Fermi liquid specific heat of each independent d orbital, that is [41]:

$$\gamma_i^m \propto \frac{\rho_i^m(\epsilon_F)}{Z_{d,i}^m}, \quad (19)$$

where ϵ_F is the Fermi energy, and it follows:

$$Z_{d,i} = \sum_m \rho_i^m(\epsilon_F) / \sum_m \gamma_i^m. \quad (20)$$

The effect of the localization induced by disorder can be quantized by the average Z_d , which is obtained along the same lines:

$$Z_d = \sum_i \rho_i(\epsilon_F) / \sum_i \gamma_i. \quad (21)$$

Z_d is related to the mass renormalization ($Z_d = m/m^*$).

COMPARISON BETWEEN THE ED AND CTQMC IMPURITY SOLVERS

In this section, we extend the discussion of the single site DMFT results for VO_2 . We first discuss the Matsubara representation of the Green's function (the real and imaginary parts of the Green's function are shown respectively in Fig. 2.a and Fig. 2.b.) We obtained, in particular, that the orbital density at the Fermi level $n = -G''(i\omega_n = 0)/\pi$ obtained by CTQMC (open symbols) is largest for the d_{xy} orbital. Interestingly, we find that the e_g states are almost empty and do not have a significant weight at the Fermi level. The case for such an orbital selection process was argued long ago by Goodenough [42]: VO_2 can be regarded as a $3d^1$ system in the simple ionic picture (with full charge transfer from the V $3d^3 4s^2$ to the two O $2p^4$ configurations). The low energy states near the Fermi level are of strong vanadium 3d character and each vanadium atom is surrounded by an oxygen octahedron, such that the crystal field splits the 3d states into t_{2g} and e_g bands. Since the structure is not cubic, however, the t_{2g} states are further split into $e_{\pi g}$ and a_{1g} states. In this simple ionic picture, the remaining 3d electron partially occupies the a_{1g} band and the system remains metallic in the rutile phase. In the M_1 phase, pairs of vanadium atoms along the rutile axis form dimers. This Peierls distortion causes strong hybridization between the a_{1g} orbitals of the two vanadium atoms, allowing the bonding state to fully fill and opening a gap between the bonding a_{1g} and the unoccupied π bands.

While the t_{2g} orbitals point between the oxygen sites, the $d_{x^2-y^2}$ and $d_{3z^2-r^2}$ orbitals point towards the oxygen sites, giving strong σ -bonds with the O 2p orbitals: because of the high electronegativity of oxygen (3.5) compared to vanadium (1.6), the bonding $d_{3z^2-r^2}$ and $d_{x^2-y^2}$ orbitals are of mainly O 2p character and hence the electrons are more localized to the O 2p than the V 3d orbitals; an almost ideal ionic bond. This suggests that the most localized orbitals in the 3d shell are the t_{2g} , and that polarized X-ray spectroscopy mainly resolves t_{2g} orbitals at the vanadium sites.

This scenario is also supported by the CTQMC data (Fig. 2.a,b), which shows that dynamic correlations effects are not important for the e_g orbitals. We obtained, from DFT+DMFT solved with the CTQMC, total densities of (0.68, 0.73, 0.52, 0.52, 0.68) respectively in the com-

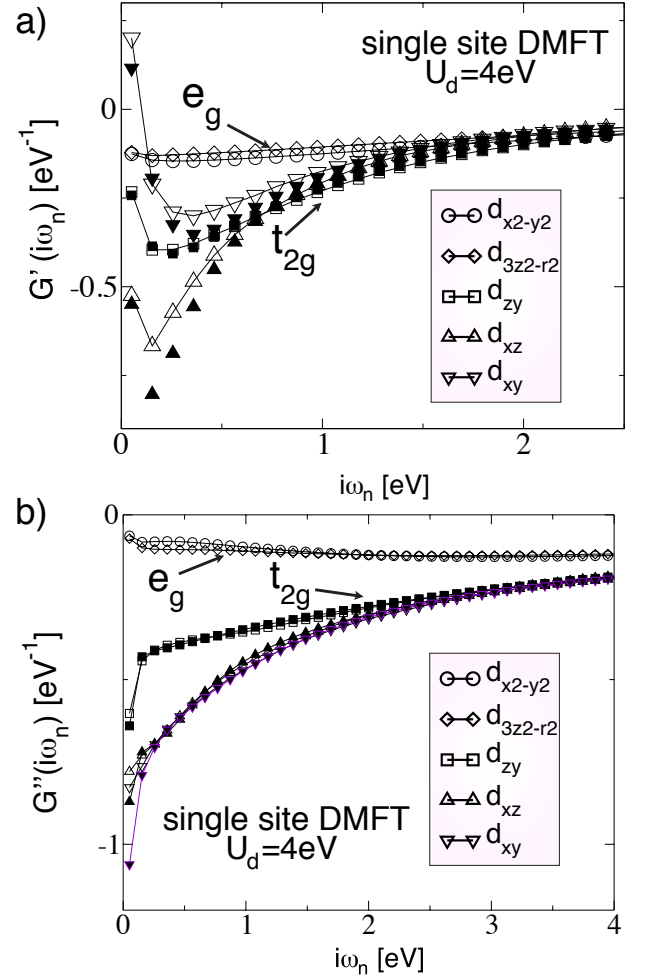


FIG. 2: **Matsubara representation of the Green's function:** (Color online) Real (a) and imaginary part (b) of the Green's function \tilde{G} in the Matsubara representation for paramagnetic VO_2 . The calculations were performed using the CTQMC impurity solver (open symbols) including all five Vanadium d orbitals (e_g and t_{2g}) are compared with the calculations performed with the ED impurity solver (filled symbols), which includes only the three t_{2g} orbitals.

ponents of the 3d subshell ($d_{x^2-y^2}, d_{3z^2-r^2}, d_{yz}, d_{xz}, d_{xy}$). Thus, there is $n = 1.4$ e in the e_g and 1.7 e in the t_{2g} orbitals, in broad agreement with the $n = 1.83$ e occupation of the 3d shell extracted from XAS measurements [43] and $n = 1.9$ e obtained using photoemission spectroscopy [44].

The real and imaginary parts of the self-energy are shown in Fig. 3.a and Fig. 3.b. The dynamical correlations, described by the imaginary part of the self-energy, show that the d_{xy} orbital is also the most correlated orbital, whereas the e_g states are weakly correlated. The latter is also supported by the weak frequency dependence of the e_g states in the real part of the self en-

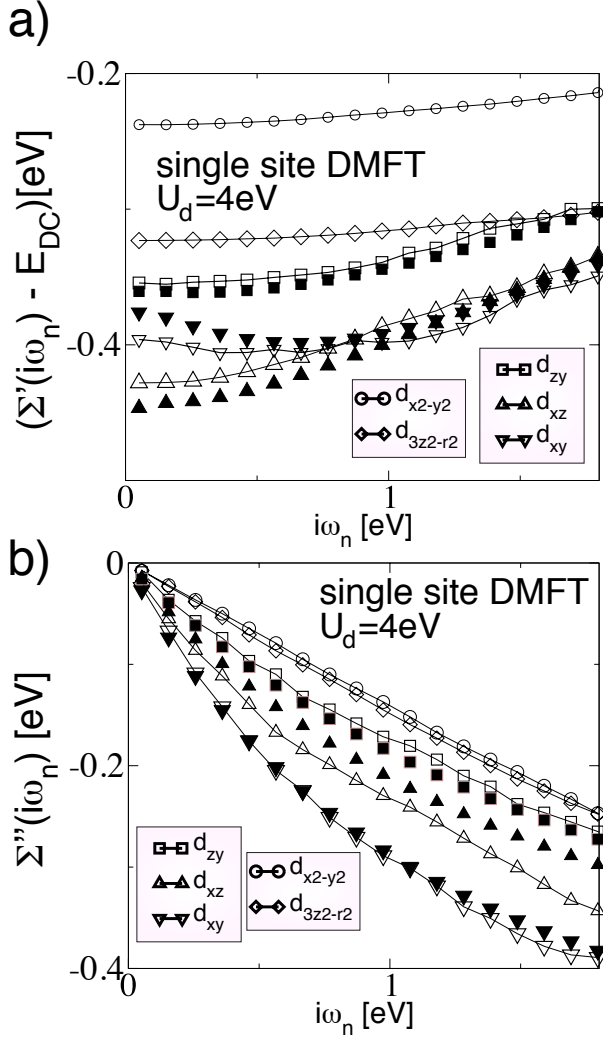


FIG. 3: **Matsubara representation of the self-energy:** (Color online) Real (a) and imaginary part (b) of the self-energy $\tilde{\Sigma}$ in the Matsubara representation for paramagnetic VO₂. The calculations performed with the CTQMC impurity solver (open symbols) including all five Vanadium d orbitals (e_g and t_{2g}) are compared with the calculations performed using the ED impurity solver (filled symbols), which includes only the three t_{2g} orbitals.

ergy (Fig. 3.a). Since the e_g orbitals do not exhibit any strong dynamical correlation, it is a good approximation to treat them at the Hartree level and thus we applied the ED solver only to the t_{2g} orbitals. We tested this approximation by comparing the densities obtained with the two methods. In particular, we obtain by using this approximation and the ED solver a total density in the t_{2g} orbital $n = 1.69$ e, in very good agreement with the CTQMC calculation, which finds a density of $n = 1.7$ e in the t_{2g} orbitals, and includes all the five d orbitals within the calculation. The comparison between the ED

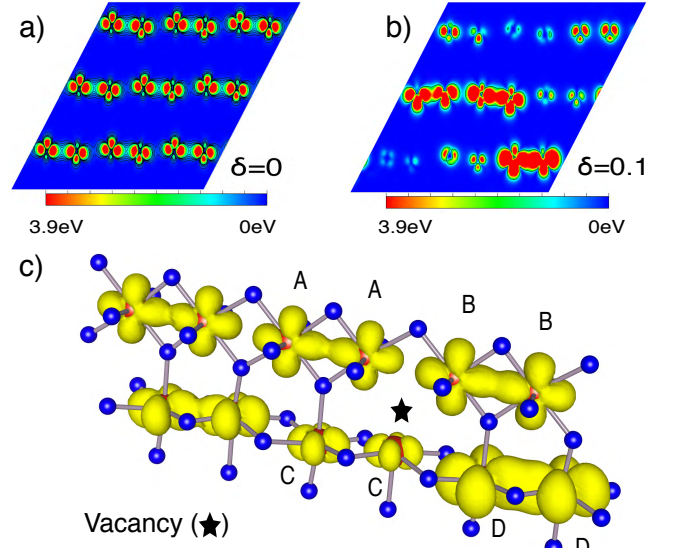


FIG. 4: **Real space representation of the scattering rate for cellular DMFT calculations:** (Color online) Contour plot of the real-space representation of the scattering rate at the Fermi level $-\Sigma''(\mathbf{r}, \mathbf{r})$ obtained by cellular DMFT (c-DMFT) shown for a [010] cut of the supercell-cell with zero (a) and finite disorder ($\delta = 0.1$ Å) (b). c) Real-space iso-surfaces of the scattering rate at the Fermi level for the case of the O vacancy (star). The large (small) spheres denote V (O) atoms. The rutile axis is oriented along the horizontal direction in all the calculations above.

(filled symbols in Fig. 2.a,b and Fig. 3.a,b) and CTQMC (open symbols in Fig. 2.a,b and Fig. 3.a,b) is remarkable for both the Green's function (Fig. 2.a,b) and self-energy (Fig. 3.a,b). Finally, we obtain also a very good agreement for the quasi-particle weight Z_d obtained with the ED ($Z_d = 0.77$) and CTQMC ($Z_d = 0.73$) solvers. The data shown in the paper and supplementary material were obtained with the ED solver when not specified otherwise.

REAL SPACE REPRESENTATION OF THE SELF-ENERGY OBTAINED BY C-DMFT

In this section, we extend the discussion regarding the cellular c-DMFT calculations under the presence of external perturbations, such as disorder and vacancies. Contour plots of the real-space representation of the local part of the scattering rate, $-\Sigma''(\mathbf{r}, \mathbf{r})$, obtained by cellular DMFT (c-DMFT), for a [010] cut of the supercell, are shown for zero and finite disorder in Fig. 4.a and Fig. 4.b, respectively. Interestingly, we find that a moderate disorder of $\delta = 0.1$ Å enhances the dimer bonding character by reducing the V-V distance among some of the dimers and thus increasing the self-energy. This is illustrated by the real-space representation of the

scattering rate, in the [010] plane, of the super-cell for $\delta = 0$ Å (Fig. 4.a) and $\delta = 0.1$ Å (Fig. 4.b). Significantly, although the bonding character of some dimers is inevitably diminished, the integrated spectral function (Fig. 3.a in the paper) shows that the Mott localization effect is strong enough to sustain an insulator, such that no spectral weight is present at the Fermi level.

A very different effect is observed for the case of a single O vacancy. At $\delta = 0$ Å, this defect does not affect the band edges but instead induces a mid-gap state with a finite weight at the Fermi level. The real-space iso-surfaces of the scattering rate show (Fig. 4.c) that the vacancy breaks a dimer (dimer C) and enhances the bonding of the nearest neighbor dimer (D). In particular, the strong mass renormalization associated with the Mott instability prevents the charge to flow freely between neighbour dimers, such that the mid-gap state remains essentially local in space. We argue that this mid-gap, localized state is relevant to the thin-film deposition of VO₂ layers, where it was recently found that the strain of the substrate might induce subtle deviation from the canonical stoichiometry, and moreover that the metal-insulator transition was strongly varied over different samples [7].

-
- [1] P. Hohenberg and W. Kohn, Phys. Rev. **136**, B864 (1964).
 - [2] W. Kohn and L. J. Sham, *ibid.* **140**, A1133 (1965).
 - [3] W. Kohn, Phys. Rev. Lett. **76**, 3168 (1996).
 - [4] N. D. M. Hine, P. D. Haynes, A. A. Mostofi, C.-K. Skylaris, and M. C. Payne, Computer Physics Communications **180**, 1041 (2009).
 - [5] D. D. O'Regan, N. D. M. Hine, M. C. Payne, and A. A. Mostofi, Accepted for publication in Phys. Rev. B (2012), arXiv/1111.5943.
 - [6] N. D. M. Hine, P. D. Haynes, A. A. Mostofi, and M. C. Payne, The Journal of Chemical Physics **133**, 114111 (2010).
 - [7] C. Chen, Y. Zhao, X. Pan, V. Kuryatkov, A. Bernussi, M. Holtz, and Z. Fan, Journal of Applied Physics **110**, 023707 (2011).
 - [8] A. M. Rappe and E. J. Walter, Opium package, <http://opium.sourceforge.net>.
 - [9] D. D. O'Regan, N. D. M. Hine, M. C. Payne, and A. A. Mostofi, Phys. Rev. B **82**, 081102 (2010).
 - [10] K. Terakura, T. Oguchi, A. R. Williams, and J. Kübler, Phys. Rev. B **30**, 4734 (1984).
 - [11] V. I. Anisimov, J. Zaanen, and O. K. Andersen, Phys. Rev. B **44**, 943 (1991).
 - [12] W. E. Pickett, S. C. Erwin, and E. C. Ethridge, Phys. Rev. B **58**, 1201 (1998).
 - [13] E. Clementi and D. L. Raimondi, The Journal of Chemical Physics **38**, 2686 (1963).
 - [14] R. McWeeny, Rev. Mod. Phys. **32**, 335 (1960).
 - [15] E. Hernández and M. J. Gillan, Phys. Rev. B **51**, 10157 (1995).
 - [16] C.-K. Skylaris, A. A. Mostofi, P. D. Haynes, O. Diéguez, and M. C. Payne, Phys. Rev. B **66**, 035119 (2002).
 - [17] A. Mostofi, P. Haynes, C. Skylaris, and M. Payne, Journal of Chemical Physics **119**, 8842 (2003).
 - [18] C. Skylaris, P. Haynes, A. Mostofi, and M. Payne, Journal of Chemical Physics **122** (2005).
 - [19] D. D. O'Regan, M. C. Payne, and A. A. Mostofi, Phys. Rev. B **83**, 245124 (2011).
 - [20] J. C. Slater, Phys. Rev. **49**, 537 (1936).
 - [21] J. Kanamori, Journal of Physics and Chemistry of Solids **10**, 87 (1959).
 - [22] M. Imada, A. Fujimori, and Y. Tokura, Rev. Mod. Phys. **70**, 1039 (1998).
 - [23] M. Korotin, N. Skorikov, and V. Anisimov, The Physics of Metals and Metallography **94**, 17 (2002).
 - [24] W. E. Pickett, S. C. Erwin, and E. C. Ethridge, Phys. Rev. B **58**, 1201 (1998).
 - [25] A. Georges, G. Kotliar, W. Krauth, and M. J. Rozenberg, Rev. Mod. Phys. **68**, 13 (1996).
 - [26] C. J. Bolech, S. S. Kancharla, and G. Kotliar, Phys. Rev. B **67**, 075110 (2003).
 - [27] D. Zgid and G. K.-L. Chan, Journal of Chemical Physics **134** (2011).
 - [28] V. S. Oudovenko, G. Pálsson, K. Haule, G. Kotliar, and S. Y. Savrasov, Phys. Rev. B **73**, 035120 (2006).
 - [29] G. Kotliar, S. Y. Savrasov, G. Pálsson, and G. Biroli, Phys. Rev. Lett. **87**, 186401 (2001).
 - [30] M. Capone, L. de' Medici, and A. Georges, Phys. Rev. B **76**, 245116 (2007).
 - [31] A. Liebsch and N.-H. Tong, Phys. Rev. B **80**, 165126 (2009).
 - [32] C. Weber, C. Yee, K. Haule, and G. Kotliar, arXiv/1108.3028.
 - [33] P. Werner, A. Comanac, L. de' Medici, M. Troyer, and A. J. Millis, Phys. Rev. Lett. **97**, 076405 (2006).
 - [34] K. Haule and G. Kotliar, Phys. Rev. B **76**, 104509 (2007).
 - [35] K. Haule, C.-H. Yee, and K. Kim, Phys. Rev. B **81**, 195107 (2010).
 - [36] T. Pruschke and M. Zöfl, in *Advances in Solid State Physics* **40**, Vol. 40, edited by B. Kramer (Springer Berlin / Heidelberg, 2000) pp. 251–265.
 - [37] V. Eyert, Ann. Phys. (Leipzig) **11**, 650 (2002).
 - [38] J. Ivanic and K. Ruedenberg, The Journal of Physical Chemistry **100**, 6342 (1996).
 - [39] A. J. Millis, Strong Interactions in Low Dimensions, Physics and Chemistry of Materials with Low-Dimensional Structures. **25**, 195 (2004).
 - [40] V. Halpern and A. Bergmann, Journal of Physics C: Solid State Physics **5**, 1953 (1972).
 - [41] T. Das, R. S. Markiewicz, and A. Bansil, Physical Review B **81**, 184515 (2010).
 - [42] J. B. Goodenough, J. Solid State Chem. **3**, 490 (1971).
 - [43] M. W. Haverkort, Z. Hu, A. Tanaka, W. Reichelt, S. V. Streltsov, M. A. Korotin, V. I. Anisimov, H. H. Hsieh, H.-J. Lin, C. T. Chen, D. I. Khomskii, and L. H. Tjeng, Phys. Rev. Lett. **95**, 196404 (2005).
 - [44] R. Zimmermann, P. Steiner, R. Claessen, F. Reinert, S. Hüfner, P. Blaha, and P. Dufek, Journal of Physics: Condensed Matter **11**, 1657 (1999).
 - [45] We use the Einstein convention to simplify the notations, in particular repeated Greek indices implicitly sum over the NGWFs, and as per the Einstein convention, parenthesis suspend the summation implied by matching pairs of indices.
 - [46] A fixed temperature T=189 K was used throughout all our calculations

- [47] We note that we performed the vacancy calculations with a neutral simulation cell, i.e. we did not add or remove any electrons with respect to the valence given by the norm-conserving pseudo-potentials.
- [48] Vertex-corrections vanish for a single orbital in infinite dimensions, but for all other cases this is an approximation.